


Wandering principal optical axes in van der Waals triclinic materials

Received: 16 June 2023

Accepted: 19 January 2024

Published online: 06 March 2024

 Check for updates

Georgy A. Ermolaev¹, Kirill V. Voronin², Adilet N. Toksumakov³,
Dmitriy V. Grudinin¹, Ilia M. Fradkin¹, Arslan Mazitov⁴, Aleksandr S. Slavich³,
Mikhail K. Tatmyshevskiy³, Dmitry I. Yakubovsky³, Valentin R. Solovey¹,
Roman V. Kirtaev¹, Sergey M. Novikov³, Elena S. Zhukova³, Ivan Kruglov¹,
Andrey A. Vyshnevyy¹, Denis G. Baranov³, Davit A. Ghazaryan^{3,5},
Aleksey V. Arsenin^{1,5}, Luis Martin-Moreno^{6,7}, Valentyn S. Volkov^{1,5} &
Kostya S. Novoselov^{8,9,10} 

Nature is abundant in material platforms with anisotropic permittivities arising from symmetry reduction that feature a variety of extraordinary optical effects. Principal optical axes are essential characteristics for these effects that define light-matter interaction. Their orientation – an orthogonal Cartesian basis that diagonalizes the permittivity tensor, is often assumed stationary. Here, we show that the low-symmetry triclinic crystalline structure of van der Waals rhenium disulfide and rhenium diselenide is characterized by wandering principal optical axes in the space-wavelength domain with above $\pi/2$ degree of rotation for in-plane components. In turn, this leads to wavelength-switchable propagation directions of their waveguide modes. The physical origin of wandering principal optical axes is explained using a multi-exciton phenomenological model and *ab initio* calculations. We envision that the wandering principal optical axes of the investigated low-symmetry triclinic van der Waals crystals offer a platform for unexplored anisotropic phenomena and nanophotonic applications.

Symmetry plays a pivotal role in fundamental laws of nature^{1–7}, including classical equations of motion, conservation laws, superposition principle, selection rules, and exchange interaction^{8–11}. In condensed matter, it governs many of the material's mechanical, electronic, and optical properties, such as stress tensor, electron mobility, conductivity, refractive index, and allowed nonlinear processes, among others^{12–15}. Highly symmetric atomic lattices, such as Al, Ni, and Au, result in isotropy of electronic and optical properties,

severely limiting their use^{16–18}. For instance, they lack even-harmonic generation, birefringence, and chirality^{4,19,20}. On the other hand, reducing the lattice's symmetry group leads to the emergence of anisotropy – the change of particular property in the observation direction^{5,21}. The most known consequence is the birefringence phenomenon, wherein a birefringent material doubles an image²². This effect is just one of the numerous implications of anisotropic optical properties, traditionally described via the permittivity tensor²³.

¹Emerging Technologies Research Center, XPACEO, Dubai Investment Park First, Dubai, United Arab Emirates. ²Donostia International Physics Center (DIPC), Donostia/San Sebastián 20018, Spain. ³Moscow Center for Advanced Studies, Kulakova str. 20, Moscow 123592, Russia. ⁴Institute of Materials, École Polytechnique Fédérale de Lausanne, 1015 Lausanne, Switzerland. ⁵Laboratory of Advanced Functional Materials, Yerevan State University, Yerevan 0025, Armenia. ⁶Instituto de Nanociencia y Materiales de Aragón (INMA), CSIC-Universidad de Zaragoza, 50009 Zaragoza, Spain. ⁷Departamento de Física de la Materia Condensada, Universidad de Zaragoza, 50009 Zaragoza, Spain. ⁸National Graphene Institute (NGI), University of Manchester, Manchester M13 9PL, UK. ⁹Department of Materials Science and Engineering, National University of Singapore, Singapore 03-09, Singapore. ¹⁰Institute for Functional Intelligent Materials, National University of Singapore, 117544 Singapore, Singapore. ✉ e-mail: kostya@nus.edu.sg

It effectively describes the difference in refractive indices along various directions. This anisotropy produces complex isofrequency contours in the reciprocal space²⁴ enabling hyperbolic materials²¹, ghost¹ and shear^{10,25} polaritons, negative refraction^{26,27}, canalization of radiation⁴, and many other intriguing wave phenomena.

Van der Waals (vdW) crystals offer a flexible and highly functional platform with a built-in anisotropy due to their fundamental difference between intralayer covalent and interlayer vdW bonding²⁸. Therefore, such layered materials allow exotic light-matter interactions²⁹, resulting in exciton³⁰, phonon³¹, edge³², and moiré-polaritons³³. In most cases, this anisotropy is purely uniaxial, and the principal optical axes of the permittivity tensor are stationary with wavelength²⁸. Some vdW crystals, however, have biaxial anisotropy because of the in-plane low-symmetry crystal structure^{34–38}. Combined with non-orthogonally polarized in-plane exciton resonances³⁴, rhenium disulfide and rhenium diselenide can enable the wandering (wavelength-dispersive) direction of the principal optical axes of the permittivity tensor. Although the prediction of wavelength-dispersive principal optical axes dates back to 1928³⁹, experimental evidence of the discussed behavior has been elusive in inorganic crystals. We anticipate that more exotic optical responses and applications may be expected in materials with wandering principal optical axes, which can extend the evergrowing phenomena in low-symmetry nanophotonics⁴⁰.

In this work, we experimentally observed the rotation of principal optical axes in triclinic vdW crystals. We explained it via a bi-excitonic model, also recreating the wandering of such principal optical axes with first-principle calculations of the permittivity tensor. Here, only the individual components of the obtained permittivity tensor satisfy the Kramers–Kronig (KK) relations. In contrast, the generalized KK relation for crystallographic axes⁴¹ is not applicable to triclinic rhenium disulfide (and diselenide). Hence, these crystals have extraordinary optical properties that set them apart from vdW and non-vdW crystals.

Furthermore, from a practical point of view, our near-field nanoimaging results reveal high wavelength sensitivity of light-matter interaction in triclinic vdW crystals, which can be leveraged for advanced light routing. Thus, triclinic van der Waals rhenium disulfide (and diselenide) offer a platform for anisotropic phenomena and next-generation nanophotonics.

Results

Impact of triclinic crystal structure on optical axes

ReS₂ and ReSe₂ are ideal materials for asymmetry-driven phenomena since they exhibit the lowest symmetry triclinic crystal structure⁴², shown in Fig. 1a–c. Consequently, they received considerable interest in recent works^{34–37,43–45}, which reported a high linear and nonlinear optical anisotropy originating from non-collinear excitons³⁴. In particular, the angle between the polarizations of excitons⁴⁶ is about 70° instead of the expected 90°. It arises from Peierls' distortion of the 1T structure (Fig. 1a)³⁶. This feature should, naturally, cause nontrivial optical responses, such as non-orthogonal self-hybridized polaritons⁴⁷. Therefore, a more thorough investigation of the anisotropic dielectric tensor $\hat{\epsilon}$ of ReS₂ and ReSe₂ remains a significant challenge both because their dielectric tensors cannot be diagonalized in Cartesian coordinates³⁹ and for their great demand for low-symmetry photonics.

Nevertheless, according to Onsager's theorem⁴⁸, their dielectric tensors are symmetric ($\hat{\epsilon} = \hat{\epsilon}^T$). They thus can be divided into Hermitian ($\text{Re}[\hat{\epsilon}]$) and skew-Hermitian ($\text{Im}[\hat{\epsilon}]$) parts (Fig. 1d–e), primarily responsible for polarization and losses, respectively. It is worth noting that the diagonalization basis for Hermitian and skew-Hermitian tensors can differ and vary with wavelengths, as schematically illustrated in Fig. 1d–e, which can result in wavelength-dispersive principal optical axes. In fact, principal optical axes rotation explains the effects observed in earlier reports^{35,38,49} on optical properties of ReS₂ (Supplementary Note 1).

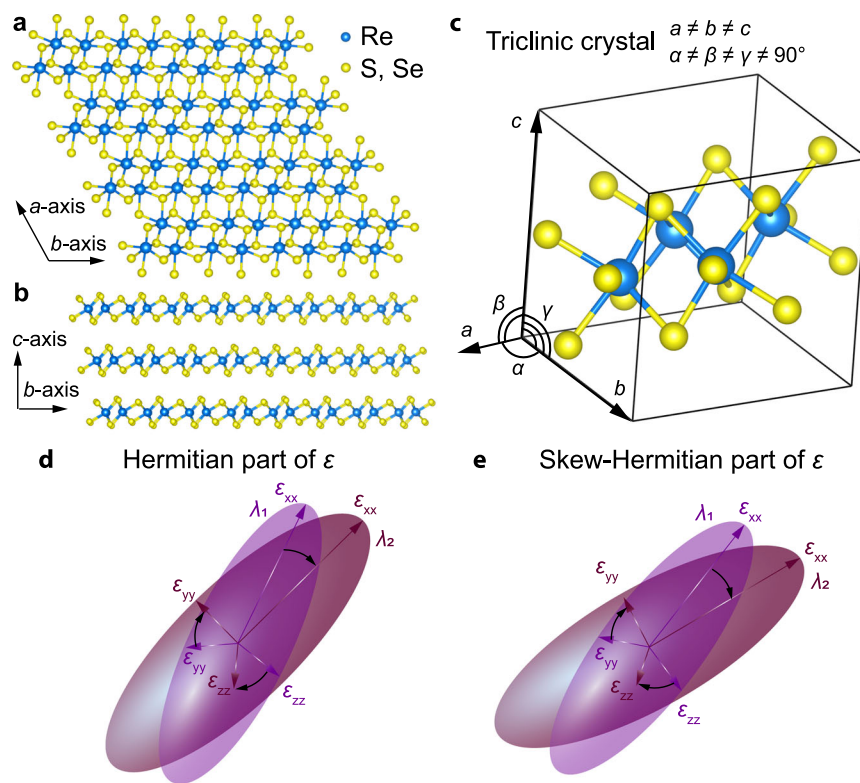


Fig. 1 | Conceptualization of wavelength-dispersive principal optical axes in triclinic crystals. Crystal structure of ReS₂ and ReSe₂ (a) along the *c*-axis and (b) along the *a*-axis. (c) three-dimensional view of the unit cell, where α , β , and γ are crystallographic angles of triclinic crystal. Schematic illustration of wandering

principal optical axes for (d) Hermitian and (e) skew-Hermitian parts of dielectric tensors. ϵ_{xx} , ϵ_{yy} , and ϵ_{zz} stands for dielectric permittivities in the basis of principal optical axes along principal optical axes for two wavelengths λ_1 and λ_2 .

Physical origins of wandering principal optical axes

To visualize this effect, we prepared ReS_2 and ReSe_2 samples (Fig. 2a, b and Supplementary Note 2) and measured polarised transmittance (Fig. 2c) around the exciton resonances. Figure 2c demonstrates how the angle for maximum transmittance shifts for different excitons, showing that the principal optical axes change with exciton resonances. In order to capture its wavelength dependence, we provide polarization spectra in Fig. 2d–e for ReS_2 and in Supplementary Note 2 for ReSe_2 . Note that excitonic spectral dips vanish at certain polarizations (Fig. 2d), indicating the orientation of excitons. Of immediate interest are wandering (wavelength-dispersive) principal optical axes, shown in Fig. 2e and Supplementary Note 2. In fact, a recent study⁵⁰ showed that the principal optical axis at 550 and 650 nm tilts by 3° and 2° , respectively, with respect to the b -axis for few-layer ReS_2 , which is close to our 7° and 8° observed for bulk ReS_2 (see Fig. 2e). At large wavelengths, the principal optical axes almost coincide with the crystallographic axes (Fig. 2e). However, the principal optical axes vary rapidly at fundamental exciton frequencies and then demonstrate complex behavior for high-energy photons, owing to the material's rich excitonic structure⁵¹. Still, the crystallographic axes influence the

position of the principal optical axes since, at the fundamental exciton resonances, the principal optical axes switch from the crystallographic b -axis to the a -axis (Fig. 2e). At infrared wavelengths, this wandering of principal optical axes reaches 65° whereas, for the whole spectral range, it exceeds 110° change, as seen in Fig. 2e.

Furthermore, this extraordinary optical response influences the Raman spectra (Supplementary Note 3). For instance, polarisation-resolved Raman measurements reveal the change of phonon modes' preferential direction when the excitation wavelength switches from 532 nm to 633 nm and then to 780 nm (Supplementary Note 3). Although phonon modes' directions have more complex behavior since they depend not only on the orientation of the principal optical axes but on the phonon modes themselves, their dispersion follows a similar pattern to principal optical axes (Supplementary Note 3). This trend is unique to ReS_2 and ReSe_2 , as we demonstrate in Supplementary Note 4, exemplifying a highly anisotropic As_2S_3 with static principal optical axes⁵². Indeed, As_2S_3 also has a reduced symmetry, which in principle, may cause a similar effect of wandering principal optical axes. However, unlike ReS_2 and ReSe_2 , the crystal structure of As_2S_3 is close to orthorhombic phase with the following crystallographic parameters⁵²:

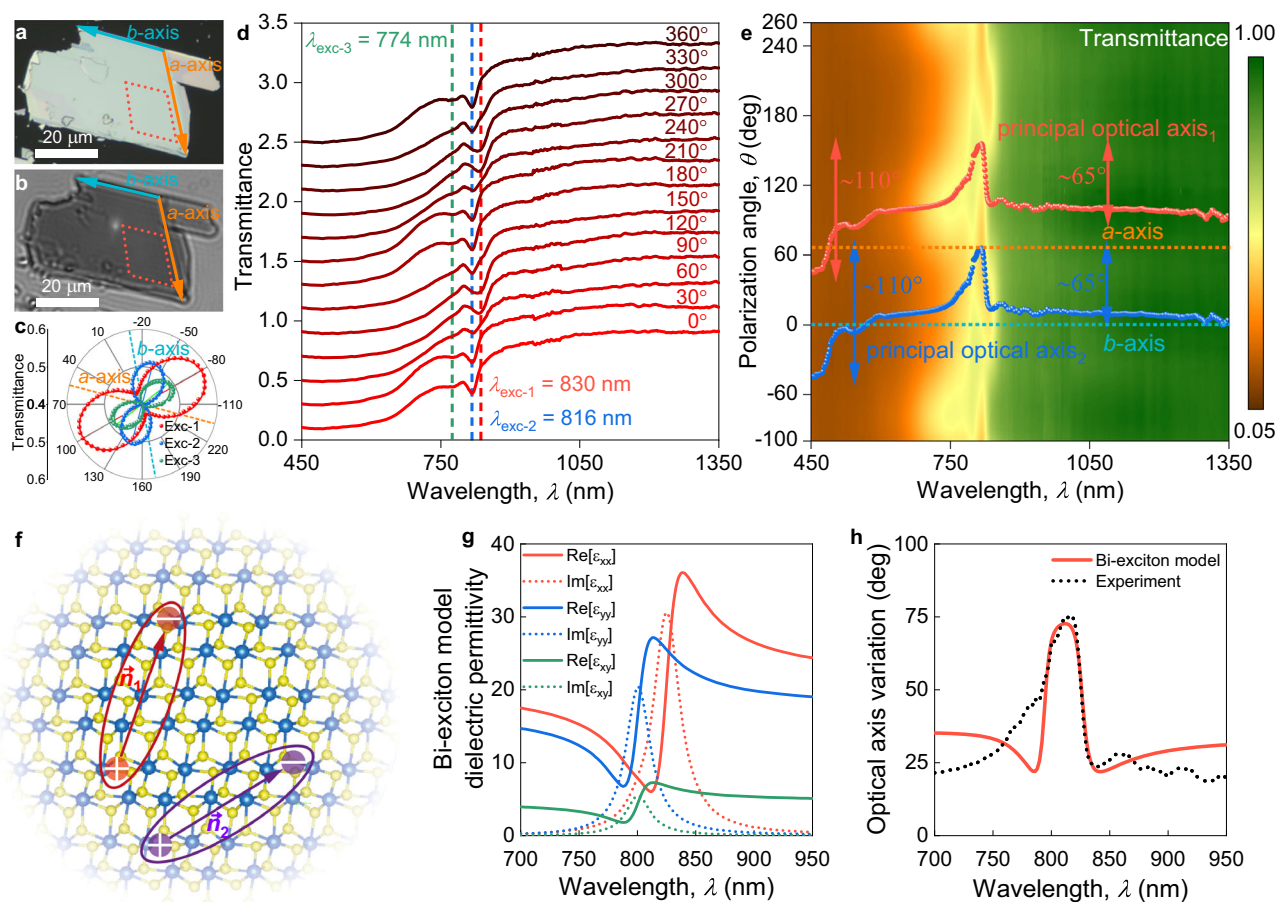


Fig. 2 | Observation of wandering (wavelength-dispersive) principal optical axes in triclinic ReS_2 . (a) Optical and (b) ellipsometry micrographs of bulk ReS_2 . Red dashed lines show the region for polarized microtransmittance measurements. (c) Polarized transmittance of bulk ReS_2 presented in panel (a), for three different exciton wavelengths of 830 nm (exc-1), 816 nm (exc-2), and 774 nm (exc-3). Each curve shifted by 0.2 for clarity. Polarized transmittance (d) spectra and (e) heat-map. In panel (d) dashed lines show the positions of fundamental excitons of bulk ReS_2 . In panel (e), red and blue points show the positions of in-plane principal optical axes. Dashed lines correspond to the crystallographic a -axis (orange line) and b -axis (cyan line). Zero degree corresponds to the crystallographic b -axis. The red and blue points are obtained through the fitting of polarization-resolved

microtransmittance at each wavelength (see Methods section Determination of principal optical axes). Arrows show the maximum position change of principal optical axes. (f) Depiction of non-orthogonal excitons (phenomenological theory). Solid lines represent the binding between electron and hole in exciton. Arrows shows the preferential direction of excitons and \mathbf{n}_1 and \mathbf{n}_2 are unit vectors describing the in-plane polarization of the corresponding excitonic transition. (g) Dielectric tensor corresponding to the bi -exciton model. Solid lines show the real parts of dielectric permittivity, while dashed lines show the imaginary parts of dielectric permittivity. (h) Principal optical axes orientation as a function of wavelength. Solid red lines show principal optical axis change predicted by bi -exciton model. Dashed line is experimental positions of principal optical axis.

$a = 0.42546(4)$ nm, $b = 0.95775(10)$ nm, $c = 1.14148(10)$ nm, $\alpha = 90^\circ$, $\beta = 90.442^\circ$, and $\gamma = 90^\circ$; because the monoclinic angle β differs from 90° by just $0.442(4)^\circ$. Moreover, As_2S_3 is transparent in the measured spectral interval (450–1350 nm) implying that its excitons lie below 450 nm, and hence, their effect is negligible⁵². In other words, an illustration of static principal optical axes in As_2S_3 highlights the nontrivial behavior of wandering principal optical axes in ReS_2 and ReSe_2 since the observed effect requires both strongly reduced crystal symmetry and the presence of material's directional resonances: in our case excitons.

The observed behavior of the principal optical axes of ReS_2 and ReSe_2 can be described with a phenomenological bi-exciton model (Fig. 2f and Supplementary Note 5). According to this model, the permittivity tensor of ReS_2 in the visible range can be expressed as:

$$\hat{\epsilon}(\omega) = \hat{\epsilon}_\infty + f_1 \frac{\omega_1^2}{\omega_1^2 - \omega^2 - i\omega\gamma_1} \mathbf{n}_1 \otimes \mathbf{n}_1^* + f_2 \frac{\omega_2^2}{\omega_2^2 - \omega^2 - i\omega\gamma_2} \mathbf{n}_2 \otimes \mathbf{n}_2^* \quad (1)$$

where $\omega_{1,2}$ is the resonant frequency of the exciton resonance, $\gamma_{1,2}$ is its non-radiative decay rate, $f_{1,2}$ is the rescaled oscillator strength, and $\mathbf{n}_{1,2} = (n_x, n_y, n_z)^T$ is a unit vector describing the in-plane polarization of the corresponding excitonic transition. By varying the parameters of the permittivity model (ω_i, γ_i, f_i), we managed to find a dielectric tensor (Fig. 2g), which reproduces the wandering effect of ReS_2 principal optical axes (Fig. 2h) within a phenomenological bi-exciton model. The satisfactory agreement between the two-exciton model and the experiment corroborates the leading role of excitons in the observed behavior.

Real-space nanoimaging of wandering principal optical axes

Wandering of ReS_2 and ReSe_2 principal optical axes opens the door to wavelength-switchable optics for efficient light manipulation. As a practical demonstration, we show the effect of wavelength-dispersive principal optical axes on waveguide mode propagation direction using a scattering scanning near-field optical microscopy (s-SNOM) in the transmission scheme, depicted in Fig. 3a. This scheme has no angular rotation (Supplementary Note 6) which makes it advantageous over the reflection scheme. Notably, the principal optical axes vary rapidly at fundamental exciton frequencies (see Fig. 2e and Supplementary Note 2). Therefore, for measurements, we focused on ReSe_2 because it provides a strong variation in the orientation of the principal optical axes within the measured wavelength range of our s-SNOM setup (Methods). To eliminate the edge effect on the near-field image when

launching the waveguide modes and launch those modes isotropically, we created a circular hole (the inset in Fig. 3a) inside the ReSe_2 sample. It allows us to visualize the asymmetry of waveguide modes (Fig. 3b–d) caused by material anisotropy only: Fig. 3b–d show elliptical light propagation. As anticipated, these ellipses rotate with wavelength change, as seen from the position of their major axes in Fig. 3e–g (theoretical background of direction change which is provided in Supplementary Notes 7–9). Notably, the observed near-field mode is an interference between the air and waveguide modes. Still, according to our analysis, the air mode's contribution to the rotation of the mode's propagation direction is negligible with respect to the wavelength (see Supplementary Note 9). Hence, wandering (wavelength-dispersive) principal optical axes offer a platform to manipulate light without additional structuring and engineering.

Anisotropic dielectric tensors with wandering optical axes

Given the strong wavelength dispersion of the principal optical axes, it is challenging to describe the optical responses of ReS_2 and ReSe_2 correctly. Hence, we fitted the polarized transmittance spectra within the isotropic approximation as the initial step (see Supplementary Note 10). This approach yields a refractive index of about 4 in the infrared range, close to earlier reports^{35,38,49}, and allows for distinguishing the fundamental excitonic transitions. In the next step, we irradiated samples with unpolarized light to obtain the optical properties averaged over polarization angles. Notably, the resulting optical constants do not follow Kramers–Kronig relations (see Supplementary Note 10) in contrast to other anisotropic vdW materials⁵³. Consequently, ReS_2 and ReSe_2 exhibit anomalous optical responses even for unpolarized light due to the wavelength-dispersive principal optical axes.

To better understand the wandering of principal optical axes, we performed first-principle calculations of monolayer, bilayer, trilayer, and bulk ReS_2 and ReSe_2 anisotropic permittivity tensors, shown in Fig. 4 and Supplementary Note 9. As expected, the off-diagonal tensor elements (Fig. 4a and g) are nonzero, and tensors are not diagonalizable on the orthogonal basis (Supplementary Note 11) because of the crystal's low symmetry. Nonetheless, we can decouple Hermitian and skew-Hermitian parts of tensors and diagonalize them separately, as shown in Fig. 4 and Supplementary Note 11. The diagonalization process also gives a diagonalization basis, which, in the case of the dielectric tensors, coincides with principal optical axes. Moreover, it allows us to directly observe a dramatic change of principal optical axes orientations from theoretical calculations (Fig. 4c–f and i–l), which

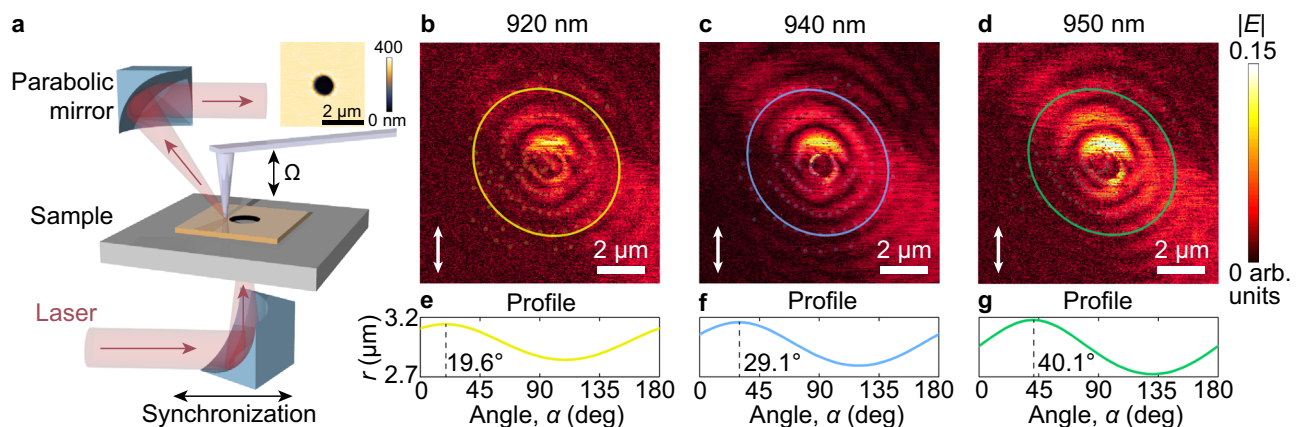


Fig. 3 | Real-space nanoimaging of wandering (wavelength-dispersive) principal optical axes in triclinic ReSe_2 . (a) Sketch of the experimental configuration for the near-field measurements in the transmission mode. The inset is a height micrograph of the hole patterned in the ReSe_2 sample. Ω is an oscillation frequency of a near-field microscope cantilever. Near-field micrographs of waveguide mode at wavelengths of (b) 920 nm, (c) 940 nm, and (d) 950 nm. Ellipses are guides to an

eye of mode propagation. Arrows indicate the incident light polarization. Dependence of the length of the radius vector of the ellipse on the angle between the radius vector and the incident polarization for (e) 920 nm, (f) 940 nm, and (g) 950 nm. The dotted line marks the angles between the ellipse's major axis and the incident polarization. The comparison of measured near-field with the calculated near-field within three-exciton model is provided in Supplementary Note 8.

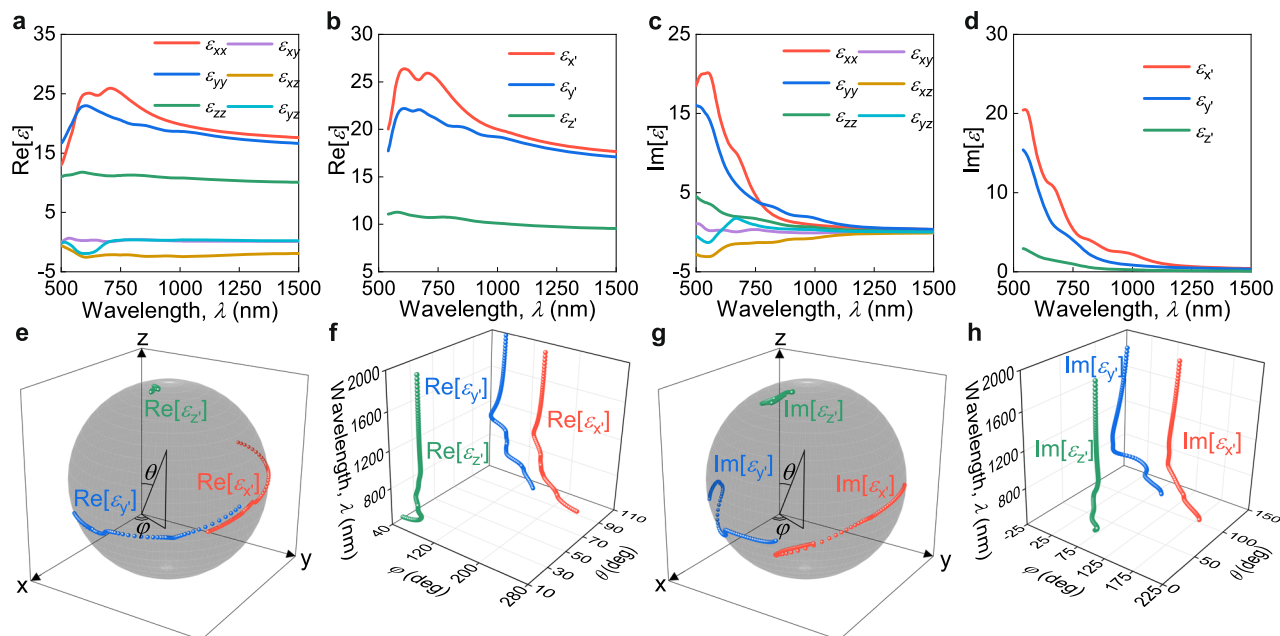


Fig. 4 | First-principle calculations of bulk ReS₂ dielectric tensor. (a) Hermitian part of the dielectric tensor. (b) Hermitian components of the dielectric tensor after the diagonalization process. (c) Skew-Hermitian part of the dielectric tensor. (d) Skew-Hermitian components of the dielectric tensor after the diagonalization process. (e) Three-dimensional view of principal optical axes variation for the Hermitian part of the dielectric tensor. Axes are dimensionless and serve as a reference for eyes. Grey sphere is also a guideline for eyes. (f) Wavelength

dependence of principal optical axes positions for the Hermitian part of the dielectric tensor in polar coordinates (φ , θ in panel (e)). (g) Three-dimensional view of principal optical axes variation for the skew-Hermitian part of the dielectric tensor. Axes are dimensionless and serve as a reference for eyes. Grey sphere is also a guideline for eyes. (h) Wavelength dependence of principal optical axes positions for the skew-Hermitian part of the dielectric tensor in polar coordinates (φ , θ in panel (g)).

agree with the experimental findings in Fig. 2, thereby unambiguously verifying the effect of wandering (wavelength-dispersive) principal optical axes in ReS₂ and ReSe₂. Moreover, the non-straight orientation of the principal optical axes of the permittivity tensor leads to slanted isofrequency surfaces with respect to the global z-axis (Supplementary Figure 21), which may enable interesting transmission phenomena, such as negative refraction and the super-prism effect⁵⁴. Hence, the unique dielectric tensors of ReS₂ and ReSe₂ (Fig. 2 and Supplementary Figure 17) provide great flexibility in optical engineering.

Discussion

The permittivity tensor is the key optical characteristic of any artificial or natural material. It describes the material's polarizability via the permittivity values and fundamental directions called principal optical axes, where birefringence is absent. Although for an overwhelming majority of inorganic materials, dielectric constant values are wavelength-dispersive, enabling numerous phenomena such as ultraslow light and Fano resonances^{55,56}, principal optical axes remain static, which limits nanophotonics since this “degree of freedom” is unavailable. In this regard, triclinic van der Waals materials offer a platform for the emergence of wandering (wavelength-dispersive) principal optical axes appearing in far- and near-fields and in quantum mechanical calculations. This unconventional optical response was demonstrated for rhenium disulfide (diselenide) and was shown to originate from non-orthogonal exciton resonances. Furthermore, the properties associated with wandering principal optical axes can be observed in fields other than optics by considering the material's non-Hermiticity arising from broken crystal symmetries. We also anticipate wandering principal optical axes in other low-symmetry crystals with triclinic and monoclinic structures, including GeS₂⁵⁷, Lu₂SiO₅⁵⁸, CdWO₄²⁵, β -phase Ga₂O₃¹⁰, and many others^{10,25,57,58}. These materials offer interesting opportunities for wavelength-switchable metamaterials, metasurfaces, waveguides, and cavities^{59–62}.

Methods

Sample preparation

Bulk ReS₂ and ReSe₂ crystals were purchased from 2D Semiconductors (Scottsdale, USA) and micromechanically cleaved down on top of required substrates (Si/SiO₂ and glass). Those substrates were subsequently decontaminated in acetone, isopropanol alcohol, and deionized water before the cleavage and then subjected to oxygen plasma removing the ambient adsorbates. Following plasma treatment, substrates were subjected to thermal treatment at temperatures of 120 °C and then exposed to scotch-tape from Nitto Denko Corporation (Osaka, Japan) with loaded bulk crystals of ReS₂ and ReSe₂. Eventually, the scotch-tape was removed, completing the cleavage procedure. The thickness of as-papered thin ReS₂ and ReSe₂ crystals was measured by an atomic force microscope (NT-MDT Spectrum Instruments, Ntegra II) in Hybrid Mode using HA_NC tips with resonant frequency of 140 kHz and spring constant of 3.5 N/m.

Determination of principal optical axes

We used polarized microtransmittance measurement technique implemented on our Accurion nanofilm_ep4 ellipsometer to determine the principal optical axes. During the measurements, we aligned the polarizer and analyzer of the ellipsometer and fitted the obtained polarized microtransmittance for each wavelength by the expression: $T(\theta, \lambda) = a^2 \cos^4(\theta - \varphi) + b^2 \sin^4(\theta - \varphi) + 2abc \cos^2(\theta - \varphi) \sin^2(\theta - \varphi) \cos(\Delta\phi)$, where $T(\theta, \lambda)$ is the polarized microtransmittance, which depends on the polarizer's/analyzer's angle θ , and the incident wavelength λ . a^2 and b^2 are the transmittances of beams polarized along in-plane principal optical axes, $\Delta\phi$ is a phase difference between transmitted rays polarized along principal optical axes, and φ indicates the angular position of the principal optical axis (see blue points in Fig. 2e), whereas another principal optical axis is given by the sum $\varphi + 90^\circ$ (see red points in Fig. 2e).

Scanning near-field optical microscopy

The fabricated hole in ReSe₂ was characterized by the amplitude- and phase-resolved scattering-type scanning near-field optical microscopy (s-SNOM) measurements using the “NeasNOM” setup (Neaspec GmbH). The s-SNOM works as an atomic force microscope (AFM) in a tapping mode with a Pt-coated silicon tip oscillating at the resonance frequency of $\Omega \approx 280$ kHz with an amplitude of ~ 50 nm. In the s-SNOM working at transmission configuration, the ReSe₂ hole is illuminated from below by a linearly polarized light at a normal angle to the sample surface focused by a bottom parabolic mirror. As a light source, we used Ti:Sapphire continuous wave tuning laser (TiC, AVESTA Lasers and Optical Systems) with fiber coupling output, working at a wavelength range of $\lambda = 700$ – 1000 nm. While mapping the near-field signal and AFM topography around the hole with a scan area of $10 \times 10 \mu\text{m}^2$, the illumination from the bottom parabolic mirror always remained aligned with the hole due to its synchronization moving with the sample during the scan. A top parabolic mirror collects the tip-scattered near-field signal and directs it into the highly sensitive photodetector. To achieve a clear near-field image, the optical background was suppressed by demodulation of the detected signal at high-order harmonic frequency $n\Omega$ ($n = 2, 3, 4$) and using an interferometric pseudoheterodyne detection scheme with a modulated reference beam via oscillating mirror. In this work, the demodulation signal at the third harmonic (3Ω) was taken, which is enough for background-free near-field detection.

First-principle calculations

Optical constants of the ReS₂ and ReSe₂ crystals were calculated within density functional theory (DFT) and GW approximation, as implemented in VASP package⁶³. First, the atomic positions of both crystals were relaxed until the interatomic forces decreased below 10^{-3} eV/Å, while their unit cells were fixed. The lattice parameters were $a = 6.378$ Å, $b = 6.417$ Å, $c = 6.461$ Å with $\alpha = 91.62^\circ$, $\beta = 119.07^\circ$, $\gamma = 105.115^\circ$ for ReS₂ and $a = 6.716$ Å, $b = 6.602$ Å, $c = 6.728$ Å with $\alpha = 104.90^\circ$, $\beta = 91.82^\circ$, $\gamma = 118.94^\circ$ for ReSe₂. Next, we obtained ground-state one-electron wavefunctions from DFT and used them to initialize the GW routines. Finally, we calculated the imaginary and real parts of the frequency-dependent dielectric function within GW approximation and derived the refractive indices and extinction coefficients of the material. The cutoff energy for the plane-wave basis was set to 500 eV, while the first Brillouin zone was sampled with a Γ -centred $6 \times 6 \times 6$ grid. The exchange correlation effects were described with a generalized gradient approximation (Perdew-Burke-Ernzerhof functional), and the behavior of wavefunctions in the core region was reconstructed with the projector augmented wave pseudopotentials.

Data availability

The relevant raw and generated data supporting the key findings of this study are available in the figshare database under accession code <https://figshare.com/s/a1edc12b21d3a36315ab> (<https://doi.org/10.6084/m9.figshare.24967593>). All data are available from the corresponding author upon a request.

References

- Ma, W. et al. Ghost hyperbolic surface polaritons in bulk anisotropic crystals. *Nature* **596**, 362–366 (2021).
- Parimi, P. V., Lu, W. T., Vodo, P. & Sridhar, S. Imaging by flat lens using negative refraction. *Nature* **426**, 404–404 (2003).
- Krishnamoorthy, H. N. S., Jacob, Z., Narimanov, E., Kretzschmar, I. & Menon, V. M. Topological transitions in metamaterials. *Science* **336**, 205–209 (2012).
- Hu, G. et al. Topological polaritons and photonic magic angles in twisted α -MoO₃ bilayers. *Nature* **582**, 209–213 (2020).
- Biswas, S., Grajower, M. Y., Watanabe, K., Taniguchi, T. & Atwater, H. A. Broadband electro-optic polarization conversion with atomically thin black phosphorus. *Science* **374**, 448–453 (2021).
- Zhang, Q. et al. Interface nano-optics with van der Waals polaritons. *Nature* **597**, 187–195 (2021).
- Gross, D. J. The role of symmetry in fundamental physics. *Proc. Natl Acad. Sci.* **93**, 14256–14259 (1996).
- Livio, M. Why symmetry matters. *Nature* **490**, 472–473 (2012).
- Schwichtenberg, J. *Physics from Symmetry*. (Springer International Publishing, 2018). <https://doi.org/10.1007/978-3-319-66631-0>.
- Passler, N. C. et al. Hyperbolic shear polaritons in low-symmetry crystals. *Nature* **602**, 595–600 (2022).
- Coissard, A. et al. Imaging tunable quantum Hall broken-symmetry orders in graphene. *Nature* **605**, 51–56 (2022).
- Tang, F., Po, H. C., Vishwanath, A. & Wan, X. Comprehensive search for topological materials using symmetry indicators. *Nature* **566**, 486–489 (2019).
- Guo, C. et al. Switchable chiral transport in charge-ordered kagome metal CsV₃Sb₅. *Nature* **611**, 461–466 (2022).
- Deb, S. et al. Cumulative polarization in conductive interfacial ferroelectrics. *Nature* **612**, 465–469 (2022).
- Yazdani, A. Magic, symmetry, and twisted matter. *Science* **371**, 1098–1099 (2021).
- Mahenderkar, N. K. et al. Epitaxial lift-off of electrodeposited single-crystal gold foils for flexible electronics. *Science* **355**, 1203–1206 (2017).
- Mason, P. E. et al. Spectroscopic evidence for a gold-coloured metallic water solution. *Nature* **595**, 673–676 (2021).
- Munkhbat, B., Canales, A., Küçüköz, B., Baranov, D. G. & Shegai, T. O. Tunable self-assembled Casimir microcavities and polaritons. *Nature* **597**, 214–219 (2021).
- Koshelev, K. et al. Subwavelength dielectric resonators for non-linear nanophotonics. *Science* **367**, 288–292 (2020).
- Tang, Y. & Cohen, A. E. Enhanced enantioselectivity in excitation of chiral molecules by superchiral light. *Science* **332**, 333–336 (2011).
- Ma, W. et al. In-plane anisotropic and ultra-low-loss polaritons in a natural van der Waals crystal. *Nature* **562**, 557–562 (2018).
- Chen, X. et al. Solution-processed inorganic perovskite crystals as achromatic quarter-wave plates. *Nat. Photonics* **15**, 813–816 (2021).
- Dressel, M. & Grüner, G. *Electrodynamics of Solids*. (Cambridge University Press, 2002). <https://doi.org/10.1017/CBO9780511606168>.
- Hu, H. et al. Doping-driven topological polaritons in graphene/ α -MoO₃ heterostructures. *Nat. Nanotechnol.* **17**, 940–946 (2022).
- Hu, G. et al. Real-space nanoimaging of hyperbolic shear polaritons in a monoclinic crystal. *Nat. Nanotechnol.* **18**, 64–70 (2023).
- Hu, H. et al. Gate-tunable negative refraction of mid-infrared polaritons. *Science* **379**, 558–561 (2023).
- Sternbach, A. J. et al. Negative refraction in hyperbolic hetero-bicrystals. *Science* **379**, 555–557 (2023).
- Ermolaev, G. A. et al. Giant optical anisotropy in transition metal dichalcogenides for next-generation photonics. *Nat. Commun.* **12**, 854 (2021).
- Basov, D. N., Asenjo-Garcia, A., Schuck, P. J., Zhu, X. & Rubio, A. Polariton panorama. *Nanophotonics* **10**, 549–577 (2020).
- Hu, F. et al. Imaging exciton-polariton transport in MoSe₂ waveguides. *Nat. Photonics* **11**, 356–360 (2017).
- Dai, S. et al. Tunable phonon polaritons in atomically thin van der Waals crystals of boron nitride. *Science* **343**, 1125–1129 (2014).
- Li, P. et al. Optical nanoimaging of hyperbolic surface polaritons at the edges of van der Waals Materials. *Nano Lett.* **17**, 228–235 (2017).
- Sunku, S. S. et al. Photonic crystals for nano-light in moiré graphene superlattices. *Science* **362**, 1153–1156 (2018).
- Aslan, O. B., Chenet, D. A., van der Zande, A. M., Hone, J. C. & Heinz, T. F. Linearly Polarized Excitons in Single- and Few-Layer ReS₂ Crystals. *ACS Photonics* **3**, 96–101 (2016).

35. Mooshammer, F. et al. In-Plane Anisotropy in Biaxial ReS₂ Crystals Probed by Nano-Optical Imaging of Waveguide Modes. *ACS Photonics* **9**, 443–451 (2022).
36. Tongay, S. et al. Monolayer behaviour in bulk ReS₂ due to electronic and vibrational decoupling. *Nat. Commun.* **5**, 3252 (2014).
37. Zhang, S. et al. Quantum interference directed chiral raman scattering in two-dimensional enantiomers. *Nat. Commun.* **13**, 1254 (2022).
38. Shubnic, A. A., Polozkov, R. G., Shelykh, I. A. & Iorsh, I. V. High refractive index and extreme biaxial optical anisotropy of rhenium diselenide for applications in all-dielectric nanophotonics. *Nanophotonics* **9**, 4737–4742 (2020).
39. Szivessy, G. Kristalloptik. in *Licht Als Wellenbewegung* 635–904 (Springer Berlin Heidelberg, 1928). https://doi.org/10.1007/978-3-642-90780-7_11.
40. Krasnok, A. & Alù, A. Low-Symmetry Nanophotonics. *ACS Photonics* **9**, 2–24 (2022).
41. Dressel, M. et al. Kramers-Kronig-consistent optical functions of anisotropic crystals: generalized spectroscopic ellipsometry on pentacene. *Opt. Express* **16**, 19770 (2008).
42. Murray, H. H., Kely, S. P., Chianelli, R. R. & Day, C. S. Structure of Rhenium Disulfide. *Inorg. Chem.* **33**, 4418–4420 (1994).
43. Küçüköz, B., Munkhbat, B. & Shegai, T. O. Boosting Second-Harmonic Generation in Monolayer Rhenium Disulfide by Reversible Laser Patterning. *ACS Photonics* **9**, 518–526 (2022).
44. Li, H. et al. Stretching ReS₂ along different crystal directions: Anisotropic tuning of the vibrational and optical responses. *Appl. Phys. Lett.* **120**, 063101 (2022).
45. Chakrabarty, D. et al. Interfacial anisotropic exciton-polariton manifolds in ReS₂. *Optica* **8**, 1488 (2021).
46. Lin, D. Y. et al. Anisotropy of Photoluminescence in Layered Semiconductors ReS₂ and ReS₂:Au. *Solid State Phenom.* **170**, 135–138 (2011).
47. Gogna, R., Zhang, L. & Deng, H. Self-Hybridized, Polarized Polaritons in ReS₂ Crystals. *ACS Photonics* **7**, 3328–3332 (2020).
48. Andrieux, D. & Gaspard, P. Fluctuation theorem and Onsager reciprocity relations. *J. Chem. Phys.* **121**, 6167–6174 (2004).
49. Munkhbat, B., Wróbel, P., Antosiewicz, T. J. & Shegai, T. O. Optical Constants of Several Multilayer Transition Metal Dichalcogenides Measured by Spectroscopic Ellipsometry in the 300–1700 nm Range: High Index, Anisotropy, and Hyperbolicity. *ACS Photonics* **9**, 2398–2407 (2022).
50. Park, J. M., Lee, S., Na, W., Kim, K. & Cheong, H. Precise Determination of Offset between Optical Axis and Re-Chain Direction in Rhenium Disulfide. *ACS Nano* **16**, 9222–9227 (2022).
51. Arora, A. et al. Highly anisotropic in-plane excitons in atomically thin and bulklike 1T'-ReSe₂. *Nano Lett.* **17**, 3202–3207 (2017).
52. Slavich, A. S. et al. Exploring van der Waals materials with high anisotropy: geometrical and optical approaches. Preprint at <https://arxiv.org/abs/2309.01989> [arxiv.org] (2023).
53. Ermolaev, G. et al. Topological phase singularities in atomically thin high-refractive-index materials. *Nat. Commun.* **13**, 2049 (2022).
54. Kosaka, H. et al. Superprism phenomena in photonic crystals. *Phys. Rev. B* **58**, R10096–R10099 (1998).
55. Tsakmakidis, K. L., Hess, O., Boyd, R. W. & Zhang, X. Ultraslow waves on the nanoscale. *Science* **358**, eaan5196 (2017).
56. Limonov, M. F., Rybin, M. V., Poddubny, A. N. & Kivshar, Y. S. Fano resonances in photonics. *Nat. Photonics* **11**, 543–554 (2017).
57. Wang, X. et al. Sub-Angstrom Characterization of the Structural Origin for High In-Plane Anisotropy in 2D GeS₂. *ACS Nano* **14**, 4456–4462 (2020).
58. Stokey, M. et al. Infrared active phonons in monoclinic lutetium oxyorthosilicate. *J. Appl. Phys.* **127**, 115702 (2020).
59. Jahani, S. & Jacob, Z. All-dielectric metamaterials. *Nat. Nanotechnol.* **11**, 23–36 (2016).
60. Liu, Y., Huang, Y. & Duan, X. Van der Waals integration before and beyond two-dimensional materials. *Nature* **567**, 323–333 (2019).
61. Datta, I. et al. Low-loss composite photonic platform based on 2D semiconductor monolayers. *Nat. Photonics* **14**, 256–262 (2020).
62. Trovatiello, C. et al. Optical parametric amplification by monolayer transition metal dichalcogenides. *Nat. Photonics* **15**, 6–10 (2021).
63. Kresse, G. & Furthmüller, J. Efficient iterative schemes for ab initio total-energy calculations using a plane-wave basis set. *Phys. Rev. B* **54**, 11169–11186 (1996).

Acknowledgements

K.S.N. acknowledges support from the Ministry of Education, Singapore (Research Centre of Excellence award to the Institute for Functional Intelligent Materials, I-FIM, project No. EDUNC-33-18-279-V12) and from the Royal Society (UK, grant number RSRP\R\190000). S.M.N. acknowledges the financial support from the Ministry of Science and Higher Education (agreement No. 075-15-2022-1150). A.S.S. and A.N.T. gratefully acknowledge the financial support from the RSF (grant No. 22-19-00558). D.A.G., A.V.A., and V.S.V. acknowledge support by the Higher Education and Science Committee of the Ministry of Education, Science, Culture, and Sport of the Republic of Armenia Project No. 23RL-2A031. L.M.M. acknowledges Project PID2020-115221GB-C41, financed by MCIN/AEI/10.13039/501100011033, and the Aragon Government through Project Q-MAD.

Author contributions

D.G.B., D.A.G., A.V.A., L. M.-M., K.S.N., and V.S.V. suggested and directed the project. G.A.E., D.V.G., A.S.S., M.K.T., D.I.Y., V.R.S., S.M.N., and E.S.Z. performed the measurements and analyzed the data. A.N.T., R.V.K., and D.A.G. prepared the samples. G.A.E., K.V.V., D.V.G., I.M.F., A.M., I.K., A.A.V., and D.G.B. provided theoretical support. G.A.E. wrote the original manuscript. G.A.E., D.G.B., D.A.G., A.V.A., L. M.-M., K.S.N., and V.S.V. reviewed and edited the paper. All authors contributed to the discussions and commented on the paper.

Competing interests

The authors declare no competing interests.

Additional information

Supplementary information The online version contains supplementary material available at <https://doi.org/10.1038/s41467-024-45266-3>.

Correspondence and requests for materials should be addressed to Kostya S. Novoselov.

Peer review information *Nature Communications* thanks the anonymous reviewers for their contribution to the peer review of this work. A peer review file is available.

Reprints and permissions information is available at <http://www.nature.com/reprints>

Publisher's note Springer Nature remains neutral with regard to jurisdictional claims in published maps and institutional affiliations.

Open Access This article is licensed under a Creative Commons Attribution 4.0 International License, which permits use, sharing, adaptation, distribution and reproduction in any medium or format, as long as you give appropriate credit to the original author(s) and the source, provide a link to the Creative Commons licence, and indicate if changes were made. The images or other third party material in this article are included in the article's Creative Commons licence, unless indicated otherwise in a credit line to the material. If material is not included in the article's Creative Commons licence and your intended use is not permitted by statutory regulation or exceeds the permitted use, you will need to obtain permission directly from the copyright holder. To view a copy of this licence, visit <http://creativecommons.org/licenses/by/4.0/>.

© The Author(s) 2024